Experimental investigation of time-invariant eddy viscosity in wave-current interaction

Xuan Zhang[a, b,c], Richard Simons[b], Eugeny Buldakov[b], Ruairi MacIver[d], Jinhai Zheng[a, c], Chi Zhang[a]

[a] College of Harbour, Coastal and Offshore Engineering, Hohai University.

[b] Department of Civil, Environmental and Geomatic Engineering, University College London, Gower Street, London, WC1E 6BT, UK.

[c] The Key Laboratory of Coastal Disaster and Defense of Ministry of Education, Hohai University.

[d] Wave Energy Scotland, An Lòchran, 10 Inverness Campus, Inverness, IV2 5NA, Scotland, UK.

Abstract: An experimental study of the turbulent boundary layer, where waves propagate with a current, is presented in this paper. A wide range of test conditions have been covered, namely, flows over a rough bed and a smooth bed, combined flows in a large-scale oscillatory water tunnel and combined waves and currents in two flumes with different scales. Particle Image Velocimetry and Laser Doppler Velocimetry were employed to obtain the velocity field. Detailed analysis of eddy viscosity profiles calculated from the experiments leads to the conclusion that previous assumed profiles do not always accurately describe eddy viscosity distributions in a combined wave-current flow. The distributions of eddy viscosity are categorised into two types (two-layer or three-layer), based on the influence of wave motions superimposed. For those cases in the current-dominated regime, eddy viscosity profiles are similar to unidirectional turbulent currents. When combined flows are in the wave-dominated regime, three-layer eddy viscosity distributions are observed. For both types, a linear eddy viscosity profile is found to be present in the bottom 10 per cent of the turbulent boundary layer. Above this, the classic parabolic profile is observed, over the whole turbulent boundary layer for the first type and over 40 per cent of the turbulent boundary layer thickness for the second type. An empirical eddy viscosity distribution in the outer region is proposed for the second type. This newly developed eddy viscosity distribution provides guidance for numerical modellers in the field of wave-current interaction and for coastal engineers wishing to predict sediment transport.

Keywords: Wave-current interaction; Laboratory experiments; Oscillating water tunnel; Wave-current flume; Eddy viscosity.

1. Introduction

The topic of wave-current interaction (WCI) has received much attention in the past few decades due to its significant applications in the field of sediment transport and marine energy exploitation. For example, prediction of sediment transport rate and coastal morphology, design of harbour structures, pipelines and tidal turbines all require a sound understanding of wave-current interaction.

Theoretical studies of WCI have emerged in parallel with developments in turbulence modelling. In order to determine mean velocity profiles and bed shear stress under a combined flow where waves propagate with a turbulent current, the Navier-Stokes (N-S) and continuity equations have been solved analytically or numerically by four main approaches: i. Direct Numerical Simulations (DNS), which solve the N-S equations directly by numerical methods without any turbulence models, and therefore motions at all scales can be obtained from the

results; ii. Large Eddy Simulations (LES), which directly calculate large-scale turbulent eddies and make approximations on small-scale ones using a subgrid-scale model (SGS model); iii. Reynolds stress models (RSM) or RANS-based models, which directly compute components of the Reynolds stress tensor through the Reynolds stress transport equations without relying on an eddy viscosity concept; iv. Eddy viscosity models using the RANS-based approach, including zero-equation models (algebraic models), one-equation models (Turbulent-Kinetic-Energy models and the Spalart-Allmaras model), and two-equation models ($k-L$ models, $k-\varepsilon$ models and $k-\omega$ models).

Due to their massive computational costs, DNS and LES have not yet been applied to practical engineering problems and are not included in the present work. The RSM approach also requires substantial computational effort and is beyond the scope of this paper. Hence, the present work is focused in particular on the eddy viscosity approximation, which is used widely by coastal engineers.

The generalised concept of eddy viscosity, being a positive scalar coefficient, was put forward by Boussinesq (1877) in analogy to molecular viscosity to relate the Reynolds stress tensor and the mean strain rate tensor. In the case of a two-dimensional mean flow, which is the case considered here (waves propagating with a turbulent current), the eddy viscosity can be defined as the coefficient of proportionality linking Reynolds shear stress with the normal velocity gradient. Dimensional analysis indicates that eddy viscosity in turbulent flows should be represented by a typical velocity scale u_m and a characteristic length scale l_m. As mentioned above, models based on eddy viscosity assumptions can be categorised into zero-equation models, one-equation models (Davies et al., 1988), and two-equation models (Son and Andre, 1991; Holmedal et al., 2003; Zheng et al., 2010; Teles et al., 2012, 2013; Zhang et al., 2014; Silva et al., 2016; and Zhang et al., 2017), depending on the number of differential equations needed to solve the length scale and/or velocity scale explicitly.

Zero-equation WCI models can be placed into four classes: time-invariant eddy viscosity (Lundgren, 1972; Grant and Madsen, 1979; Myrhaug, 1982; Christoffersen and Jonsson, 1985; Myrhaug and Slaattelid, 1989, 1990; You et al., 1991, 1992; You, 1994; Yuan and Madsen, 2015); time-dependent eddy viscosity (Malarkey and Davies, 1998); mixing length (Umeyama, 2005, 2009); and momentum (Fredsøe, 1984). A wide variety of eddy viscosity distributions have been assumed (dividing the boundary layer into two, three or four layers), together with simplified boundary layer equations, to derive mathematical representations of mean velocities and bed shear stress. A parameterised approach based on outputs from some of these models (Grant and Madsen, 1979; Fredsøe, 1984; Christoffersen and Jonsson, 1985; Myrhaug and

Slaattelid, 1990) was given by Soulsby et al., 1993 and by Holmedal et al., 2000. Most of the eddy viscosity distributions were assumed rather than obtained from experiments. There is thus scope for a validation of eddy viscosity under combined current and oscillatory flow conditions based on experiments to provide a better description of mean velocity profiles.

Results from many experimental studies have been published which provide an understanding of wave-induced changes in the mean velocity field under combined flow, either carried out in small-scale wave flumes, large-scale water tunnels, or by field tests. Laboratory results focused on a combined current and oscillatory flow have been given by Bakker and van Doorn (1978), Van Doorn (1981), Kemp and Simons (1982, 1983), Klopman (1994), Fredsøe et al. (1999), Umeyama (2005, 2009, 2011), Yuan and Madsen (2014, 2015), Musumeci et al. (2006) and Fernando et al. (2011). Field tests of bottom boundary layers in the sea have been reported by Huntley and Hazen (1988), Lambrakos et al. (1988), Soulsby and Humphrey (1990), and Trowbridge and Agrawal (1995). Bed shear stress under a combined flow has also been studied by Simons et al. (1992), Simons et al. (1994), Simons et al. (2000), Simons and MacIver (2001), and Jepsen et al. (2011). However, very few attempts have been made to use their results to validate the eddy viscosity assumptions. Existing WCI models commonly use the data from Bakker and van Doorn (1978), or Kemp and Simons (1982, 1983) for validation and there is still a need for more experimental data on WCI to cover a wider range of wave and flow conditions.

To summarise the paragraphs above, previous WCI models have relied heavily on eddy viscosity assumptions, generally describing the boundary layer in terms of different layers. Experimental studies of combined wave-current flows have been conducted to investigate the changes of flow characteristics caused by WCI, but there is no consensus as to the number, extent or shape of the layers for eddy viscosity profiles. This paper aims to provide new data, at different scales and using a range of experimental techniques, from which a relatively simple distribution of eddy viscosity can be derived, based on physical considerations and applicable to cases where the oscillatory flow is induced either by waves or in a large-scale water tunnel. The PIV measurements collected from the wave-current flume and the low-turbulence flume for smooth boundary, laminar wave conditions were used to derive the semi-empirical formula. This was validated using the data collected by LDV from the large oscillating water tunnel for rough, turbulent oscillatory flow conditions. The paper will also revisit previous formulae and make some comparisons. The results will be of use to researchers wishing to adopt a simple description for the mean velocity profile using an eddy viscosity approach (for instance, Egan et al. (2020) or Zitman and Schuttelaar (2012)).

The paper is organised into six parts as follows. Firstly, information describing the experiments is introduced in section 2. This includes descriptions of the settings required to obtain accurate experimental measurements. Section 3 presents the approach to data analysis. Next, the experimental results for the large-scale oscillating water tunnel and the smaller-scale wave-current flume are shown and the newly developed eddy viscosity distribution is presented in section 4. Section 5 discusses the influence of the newly-developed eddy viscosity distribution on the mean velocity profiles. Concluding remarks are outlined in section 6, together with some implications for numerical modellers.

2. Experimental set-up and procedures

In the present study, experiments were performed independently in three facilities: two flumes of different scale and an oscillating water tunnel. Experimental data from a range of different experimental conditions have been obtained. The overall aim is to validate existing eddy viscosity distributions and to provide a new semi-empirical formula.

2.1 Wave-current flume experiments

The first set of experiments was carried out in the UCL wave-current flume. This flume is 16m long and 0.45m wide, with glass sidewalls and bed allowing accessibility for Laser Doppler Velocimetry (LDV), Particle Image Velocimetry (PIV) and photography at the test section. The velocities at the test section were measured at the centre of the flume, using a two-dimensional PIV system. In the present study, the velocity vectors were measured in the vertical x-y plane, giving the streamwise velocities u and vertical velocities v. The PIV measurements were obtained by illuminating the vertical plane with a double-pulsed laser. The laser was fixed on a rigid steel base and produced a vertical light sheet upwards through the flume bed. For each of the conditions tested in the present study, 770 pairs of images covering an area of 195mm ×195mm were recorded consecutively. The PIV sampling frequency for the tests lay in the range 7Hz to 4Hz, depending on the wave frequency. The sampling frequency was set to aid ensemble-averaging by having an integer number of values in each wave cycle. Image processing leads to a spatial resolution of 1.5mm, which was fine enough to reveal detailed information in the bottom boundary layers. A wave probe was positioned close to the test section but not interfering with the PIV measurements, to measure the free surface elevations. Collection of the wave data was triggered by the initial firing of the first laser pulse when acquiring each set of 770 image pairs.

The experimental procedure was as follows: i. Open the valves to let the turbulent current develop and then adjust to achieve the required constant water depth; ii. Allow a settling period of 30-60 minutes before starting experiments; iii. Generate waves and wait for 50s before collecting data; iv. Stop the wave paddles. The water depth was maintained constant by an adjustable weir gate at the outlet end of the flume and adjustments of the valves. This ensures the repeatability of current conditions.

Wave properties ranged from 0.5Hz to 1Hz in frequency and from 52mm to 138mm in height, with a water depth of 0.4m. The turbulent current with a depth-averaged mean velocity of 0.175 m/s was generated and flowed with the waves in the same direction. Table 1 presents the experimental conditions of the experiments performed in the wave-current flume. The mean velocity of the unidirectional current U_c was calculated by averaging the mean velocities over depth. The wave orbital velocity amplitude U_w was calculated from wave parameters using second-order Stokes wave theory at the bed. The current Reynolds number was defined as $Re_c = U_c \cdot h/\nu$, where h is the water depth and ν is the kinematic viscosity. The wave Reynolds number based on the wave semi-orbital excursion was defined as $Re_w = U_w \cdot A_w/\nu$, where A_w is the wave semi-orbital excursion $A_w = U_w \cdot T/2\pi$ at the bed. As can be seen from the tables, current Reynolds numbers are higher than the critical number of 5000 (Sleath, 1984). Therefore, the current boundary layers are fully turbulent. Reynolds numbers of wave boundary layers based on the wave semi-orbital excursion are lower than the critical values of 1.6×10^5 as given by Sleath (1984). Therefore, the wave boundary layers for all cases lie in the laminar regime.

For more detailed information of the experimental set-up and a summary of the flow conditions, the reader is referred to Zhang and Simons, 2019. Figure 1 demonstrates the flow regimes for all the tests conducted in the wave-current flume.

Table 1. Flow conditions for experiments conducted in the wave-current flume, water depth $h = 400mm$.

Test Name	Flow Type	T (s)	H (mm)	U_c (m/s)	U_w (m/s)	Re_c	Re_w	$U_{cw} = U_c/(U_c + U_m)$
CAA	Current-only			0.175	--	71200	--	1.00
WCAAT2sA70mm	Wave-current condition	2.00	83		0.204		13546	0.46
WCAAT1.67sA120mm	Wave-current condition	1.67	120		0.266		23194	0.40
WCAAT1.43sA120mm	Wave-current condition	1.43	138		0.269		16573	0.39
WCAAT1.25sA100mm	Wave-current condition	1.25	110		0.184		7119	0.49
WCAAT1.11sA86mm	Wave-current condition	1.11	83		0.117		3138	0.60
WCAAT1sA70mm	Wave-current condition	1.00	52		0.061		1033	0.74

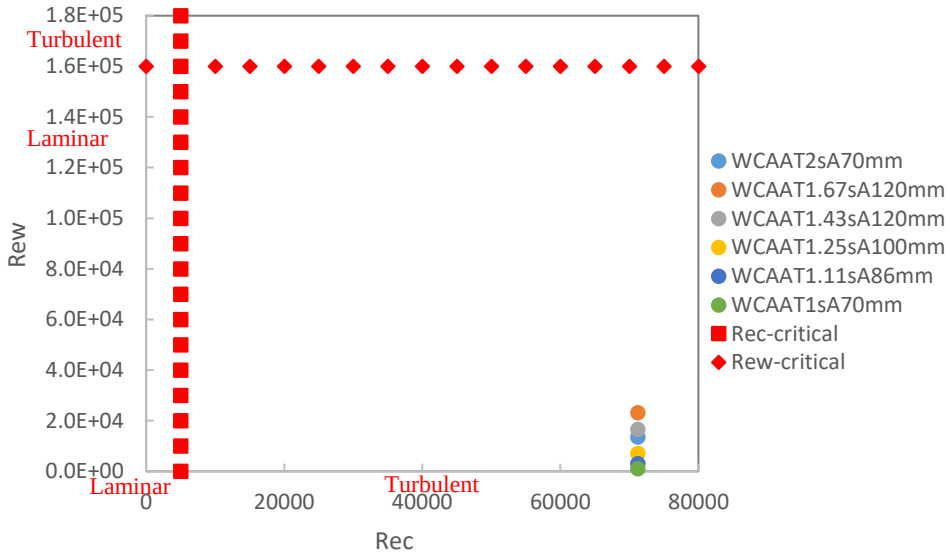

Figure 1. Diagram of the flow regimes for the tests conducted in the wave-current flume.

2.2 Low-turbulence flume experiments

The second set of experiments was conducted in the UCL low-turbulence flume. This is 6m long, 49.3 cm wide, 27 cm deep, fitted with a vertical plunger wave generator, and is described in Zhang and Simons (2019). The current generated had a depth-averaged mean velocity of 0.2 m/s. Waves were generated and propagated with the turbulent current, with wave properties ranging from 0.9Hz to 0.6Hz in frequency and wavemaker stroke up to 20mm. Test procedures were similar to those described above. Table 2 summarises the experimental conditions of the experiments performed in the low-turbulence flume. Figure 2 demonstrates the flow regimes for all the tests conducted in the low-turbulence flume. As shown in the figure, the current boundary layers are fully turbulent and the wave boundary layers for all cases lie in the laminar regime.

Table 2. Flow conditions for experiments conducted in the low-turbulence flume, water depth $h = 160mm$.

Test Name	Flow Type	T (s)	H (mm)	U_c (m/s)	U_w (m/s)	Re_c	Re_w	U_{cw}
CA	Current-only	--	--	0.200	--	32000	--	1.00
WCAT1.11sA12mm	Wave-current condition	1.11	9		0.029		154	0.87
WCAT1.11sA14mm			11		0.035		221	0.85
WCAT1.11sA18mm			14		0.046		378	0.81
WCAT1.25sA14mm	Wave-current condition	1.25	11		0.039		314	0.84
WCAT1.25sA16mm			13		0.045		405	0.82
WCAT1.25sA18mm			14		0.049		482	0.80
WCAT1.25sA20mm			16		0.056		634	0.78
WCAT1.38sA12mm	Wave-current condition	1.38	11		0.042		397	0.83
WCAT1.38sA14mm			13		0.049		532	0.80
WCAT1.38sA16mm			15		0.055		691	0.78
WCAT1.38sA18mm			15		0.058		747	0.78
WCAT1.38sA20mm			18		0.066		986	0.75
WCAT1.67sA14mm	Wave-current condition	1.67	11		0.042		482	0.83
WCAT1.67sA16mm			12		0.048		624	0.81
WCAT1.67sA18mm			14		0.055		806	0.78

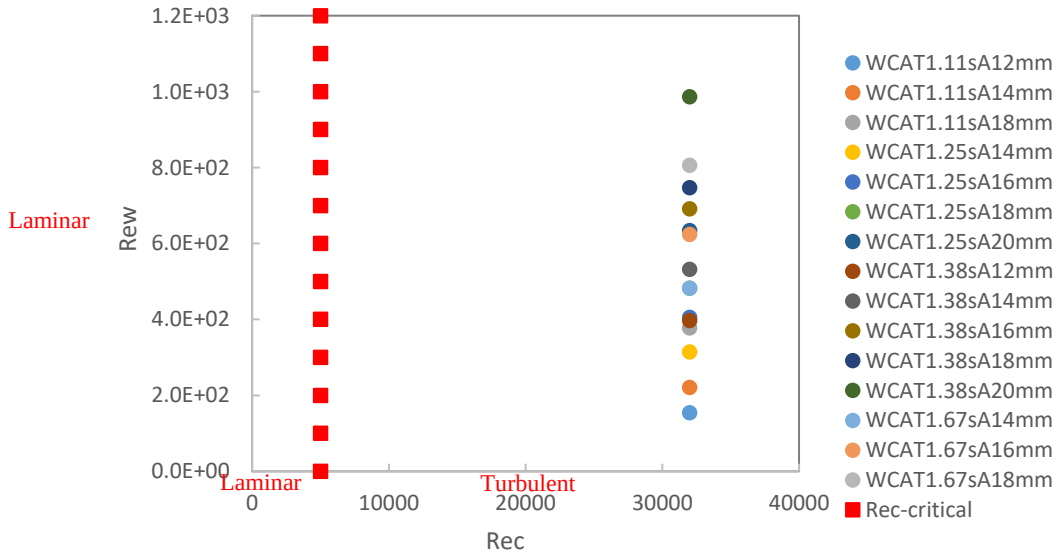

Figure 2. Diagram of the flow regimes for the tests conducted in the low-turbulence flume.

2.3 Large oscillating water tunnel experiments

The third set of experiments were carried out in the Large Oscillating Water Tunnel (LOWT) at the De Voorst Laboratory of Delft Hydraulics. The oscillating water tunnel had a working section of length 14m, a height of 1.1m, a width of 0.3m, and with cylindrical risers at each end – see Figure 3. A steel piston was located at one end of the water tunnel and was used to generate the desired oscillatory water motions, with a maximum excursion length of 4.9m at the test section. The maximum velocity amplitude was up to 1.8m/s for a wide range of wave periods

from 2.0s to 14.0s. A steady turbulent current was generated by two pumps, with capacities of 20 L/s and 100 L/s. The recirculating flow system was connected to the cylindrical risers and could be isolated from the tunnel by valves. For pure oscillatory flow tests, these valves were closed. The maximum capacity of the pump (100 L/s) corresponds to a depth-averaged velocity of 0.42 m/s. Flow straighteners were placed at both ends of the water tunnel, and the current flow was from the closed riser to the open riser.

The working section of the tunnel bed was covered with a 2D 'k-type' roughness, which was composed of 6mm square by 300mm long elements and positioned evenly with a spacing of 25mm (see Figure 4). The Nikuradse equivalent sand roughness k_s was determined from the mean horizontal velocity profile of the combined flow using the definition $k_s = 30 * y_0$. Here, y_0 represents the bed roughness and was determined from the logarithmic law of the wall:

$$\frac{\bar{U}}{u_*} = \frac{1}{\kappa} \ln\left(\frac{y}{y_0}\right) \qquad \text{……………………………………………} \quad (1)$$

where u_* represents the shear velocity (u_{*c} and u_{*wc} represent the shear velocity for current-alone test and combined wave-current tests respectively). It should be noted that the progressive origin shift method of Clauser (1956) was adopted to obtain an accurate determination of y_0 from the mean velocity profile. The origin shift ε was varied until a best fit of Equation (1) to the data in the logarithmic region of the boundary layer was achieved. The lower and upper limits of the logarithmic region were chosen in accordance with previous literature (for instance, Stuart, 1984; Perry and Joubert, 1963). This indicates a value of $k_s = 30 * y_0 = 0.0366$m.

The coordinate system adopted in the present paper had the x-direction in the direction of the mean current. The y-axis was directed upward vertically, with $y = 0$ being at the roughness element top. It should be noted that this was not the location where the mean velocity is equal to zero. The position where mean velocity is zero is a distance ε below the nominal location of y=0. Previous studies of turbulent boundary layers using 2-dimensional roughness elements (e.g. Perry et al., 1969) have found values for the velocity origin shift ε of between $0.7k$ and $0.8k$ below the roughness crest level, where k is the roughness element height. The value was observed to be $0.51k$ in the present study, in agreement with classical theories. The z-axis represents the horizontal spanwise direction across the tunnel.

The instantaneous bed shear stress was measured by a shear cell, as described by Simons and MacIver (2001). The method is based on measuring the total force on an active plate and therefore directly measures shear stress under a combined flow condition. Two velocity components were measured by LDV at 100Hz sampling rate. The duration of the sampling time was long compared with the time scales of the characteristic wave and turbulent current. This

was done to ensure a reliable time-averaged mean value for velocity and shear stress, not biased by the phase of the wave or short-term turbulent fluctuations. Sampling durations were typically of the order of a hundred wave cycles (Table 3). The different sampling durations ensured statistically reliable data for the different periods of oscillation but was otherwise not critical. Successful measurements of velocities very near the bed were accomplished by aligning the two reference beams parallel to the channel bed with the main beam directed towards the bed. The LDV measurements gave two orthogonal velocity components at an angle of $\pm 45°$, which could be processed into u- and v- velocities.

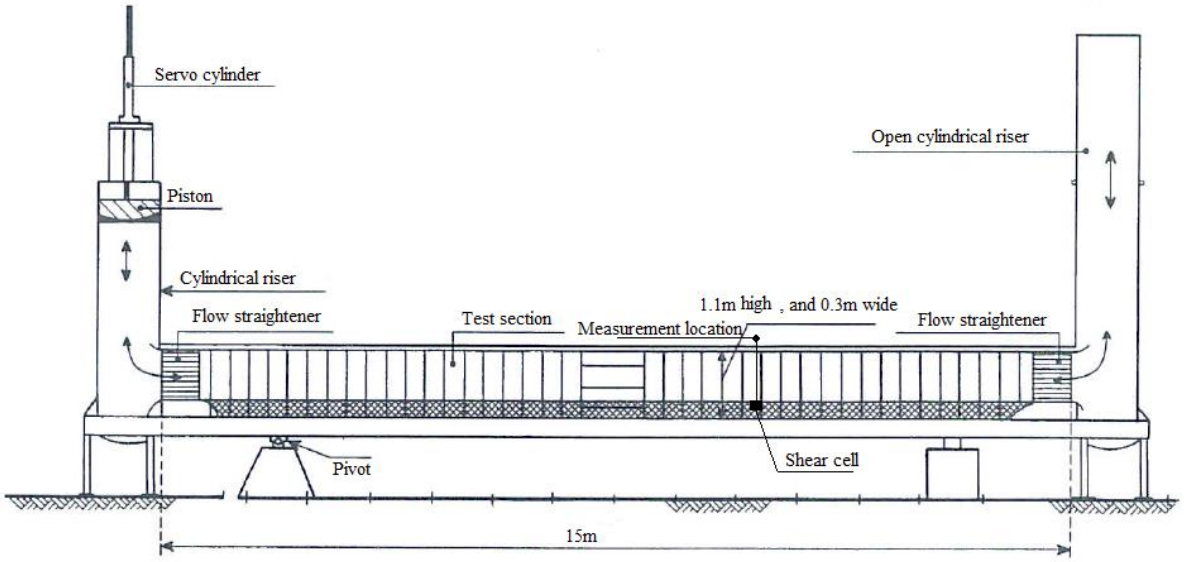

Figure 3. The Large Oscillating Water Tunnel.

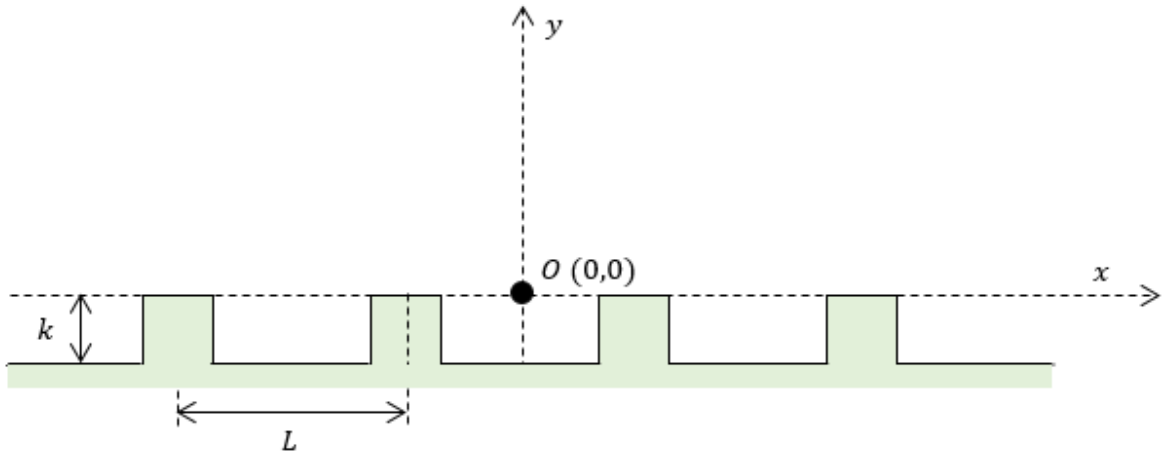

Figure 4. The idealised 2D bed roughness: $k = 6mm, L = 25mm$.

The procedure for performing a test was as follows: i. Record the start-zero reference file; ii. Generate the required test conditions in the tunnel; iii. Start data acquisition after allowing a settling time of 10-15 min; iv. Stop tunnel and allow a settling time of 10-15min; v. Record the end-zero reference file.

The experiments performed in the oscillating water tunnel covered a large range of oscillatory Reynolds number $Re_w = U_w a_w/\nu$, where U_w is the free-stream ensemble averaged velocity amplitude of the 1st harmonic measured at the outer edge of the turbulent boundary layer (y=210.6mm), a_w is the orbital amplitude, and ν is the kinematic viscosity of water determined from the water temperature. Another important non-dimensional parameter influencing the turbulent oscillatory boundary layer is the relative roughness a_w/k_s, where k_s is the Nikuradse roughness. The test conditions are listed in Table 3. It should be noted that δ_{TBL} represents the turbulent boundary layer thickness of the unidirectional current. The value of δ_{TBL} was determined as the displacement above the bed where the Reynolds shear stress goes to zero. Figure 5 demonstrates the flow regimes for all the tests conducted in the oscillating water tunnel. Noting that the critical value of wave Reynolds number over rough beds was calculated based on Equation 2.7 from Sleath (1984). As can be seen from the table and the figure, the current boundary layers are fully turbulent and the wave boundary layers for all cases lie in the turbulent regime.

Table 3. Flow conditions for the LDV velocity profile measurements ($k_s = 0.0366m$), water depth $h = 0.8$m, current free-stream velocity $U_{\infty c} = 0.51\ (m/s)$, depth-averaged mean velocity $U_c = 0.42$ (m/s), current Reynolds number $Re_c = U_{\infty c}\delta_{TBL}/\nu$ =102,000.

Case condition	Case number	T (s)	U_c or U_w at $y = 210.6mm$ (m/s)	a_w (m)	a_w/k_s	Wave Reynolds number Re_w	Data sample length (s)	$U_{cw} = U_{\infty c}/U_{\infty cw}$
C	--	--	0.5100	--	--		180	1
W	2	4.00	0.3806	0.2423	6.63	71,628	100T	0
	3	4.00	0.7894	0.5025	13.73	307,647	100T	
	4	7.75	0.3987	0.4918	13.44	152,052	40T	
	6	6.25	--	--	--	--	100T	
	8	4.50	--	--	--	--	110T	
	10	6.00	--	--	--	--	100T	
	11	9.50	--	--	--	--	100T	
WC	2	4.00	0.3844	0.2477	6.69	72,950	100T	1.33
	3	4.00	0.7884	0.5019	13.71	306,868	100T	0.65
	4	7.75	0.3861	0.4762	13.01	142,594	80T	1.32
	5	2.75	0.5465	0.2392	6.54	101,371	120T	0.93
	6	6.25	0.3574	0.3555	9.71	98,534	175T	1.43
	8	4.50	0.4941	0.3539	9.67	135,594	110T	1.03
	10	6.00	0.4714	0.4502	12.30	164,562	100T	1.08
	11	9.50	0.4125	0.6237	17.04	199,513	100T	1.24

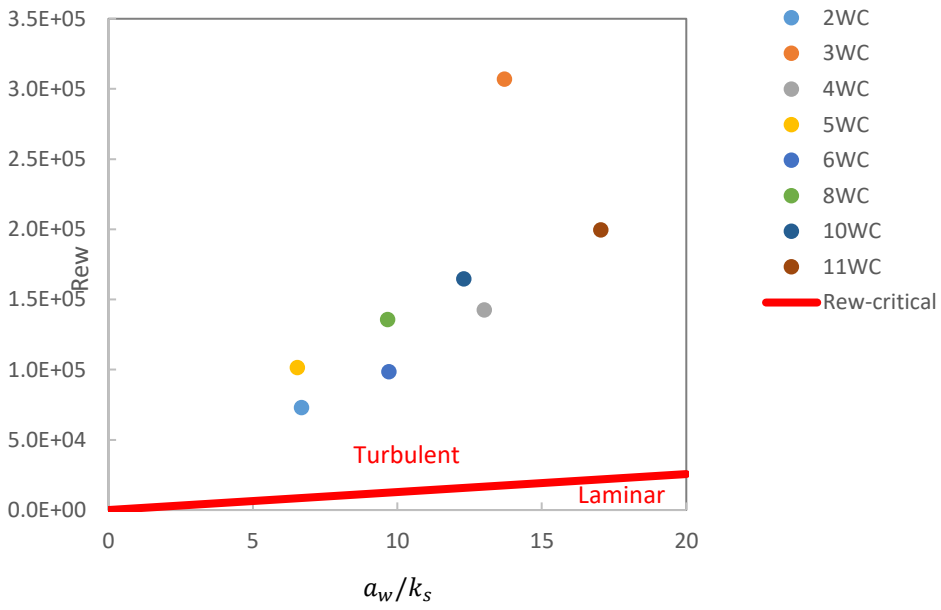

Figure 5. Diagram of the flow regimes for the tests conducted in the Large Oscillating Water Tunnel.

3. Data analysis method

It should be noted here that this paper is concerned only with the time-averaged mean flow kinematics (i.e. velocities and Reynolds shear stresses). Therefore, only the time-averaged components of eddy viscosity are calculated, and shear stresses due to periodic components are not presented. Methods for data analysis are described in the following sub-sections.

3.1 Turbulent fluctuations

In a combined wave and current condition, velocities are composed of wave-induced periodic components, a steady current-induced component and random turbulence fluctuations (Kemp and Simons, 1982; Nielsen, 1992). For a velocity component M (either u or v), this is expressed by the following equation:

$$\mathrm{M} = \mathrm{M}' + \langle \mathrm{M} \rangle \quad (2)$$

$$\langle M \rangle = \bar{M} + \widetilde{M} \quad (3)$$

$$\bar{M} = \frac{1}{N_1} \sum_{j=0}^{N_1-1} M(j \cdot dt) \quad (4)$$

$$\widetilde{M}(t) = \frac{1}{N_2} \sum_{j=0}^{N_2-1} M(t + j \cdot T) - \bar{M}, \quad 0 \le t < T \quad (5)$$

where M' is the turbulence component, $\langle M \rangle$ is the sum of periodic and time-averaged velocity component, $\bar{M}$ is the time-average of M over the full sample period, N_1 represents the whole

number of measurements for time-averaging, dt is the time between two consecutive measurements: $dt = 1/f$, f is sampling frequency, $\widetilde{M}$ is the periodic component, T is the wave period, and N_2 is the whole number of periods for ensemble-averaging.

3.1.1 Data analysis for LDV measurements

For the experimental data obtained in the large oscillating water tunnel, velocity components were measured by LDV. Because of the single-point measurement techniques adopted, the definitions given above can be applied directly for the calculations of velocity fluctuations.

3.1.2 Data analysis for PIV measurements

Each PIV image has 127 grid points in the x direction. The procedure of performing ensemble-averaging was different from the single-point measurement techniques. Three-point spatial averaging was performed first, providing high frequency smoothing. This covered a length of 4.5mm, which was much smaller than the wavelength. Thus, the difference in wave-induced velocities within the adjacent three points was negligible. Then, ensemble-averaged velocities were obtained by averaging velocities at the same wave phase over 77 or 154 cycles. The difference in the number of wave cycles for ensemble-averaging was a consequence of a different sampling frequency, which was adjusted to ensure an integer number of values of velocity in each wave cycle. These two steps can be mathematically represented by the following equations:

$$M_{new}(x_i, y, t) = \frac{1}{3}\left[M(x_{i-1}, y, t) + M(x_i, y, t) + M(x_{i+1}, y, t)\right], \quad 1 < i < 127 \quad \text{.....(6)}$$

$$< M(x_i, y, t) > = \frac{1}{N_2}\sum_{j=0}^{N_2-1} M_{new}(x_i, y, t + j \cdot T), \qquad 0 < t < T \quad \text{.....(7)}$$

where M is either the streamwise or vertical velocity component (u or v), i is the index number of longitudinal position in each PIV image, N_2 is the total number of wave cycles, y is the vertical coordinate, t is the time.

The turbulence fluctuations are expressed as:

$$M(x_i, y, t)' = M(x_i, y, t) - < M(x_i, y, t) > \quad \text{.....(8)}$$

3.2 Reynolds shear stress

3.2.1 Data analysis for LDV measurements

Having obtained the time histories of turbulence fluctuations, the Reynolds shear stress was determined by time-averaging. This is valid for the turbulent current flow with and without waves superimposed:

$$\overline{\tau_{Rey}}(y) = -\frac{1}{N_1}\sum_{n=0}^{N_1-1}\rho \cdot u'(y, n \cdot dt) \cdot v'(y, n \cdot dt) \quad (9)$$

where $\overline{\tau_{Rey}}(y)$ represents the vertical distribution of Reynolds shear stress, and ρ is the water density.

3.2.2 Data analysis for PIV measurements

For the PIV data, the Reynolds shear stress is obtained by time-averaging and spatial-averaging. Spatial averaging was used as described above to reduce noise in the data. The turbulent eddies with most energy are significantly larger than the 4.5mm over which the spatial averaging is done, so the effect on turbulence intensity is negligible. Differences in the longitudinal distributions of Reynolds shear stress are also small, and therefore spatial averaging of PIV images along the horizontal axis is adopted in the present work. The data analysis again follows the previous study of Zhang and Simons (2019).

3.3 Mean velocity profiles

The vertical distribution of mean velocity $\overline{U}(y)$ for the LDV measurements was obtained by time-averaging:

$$\overline{U}(y) = \frac{1}{N_1}\sum_{n=0}^{N_1-1} u(y, n \cdot dt) \quad (10)$$

The vertical distribution of mean velocity $\overline{U}(y)$ for the PIV measurements was obtained by time-averaging and spatial-averaging.

The mean velocity gradient was determined from the time-averaged mean velocity profile using discrete experimental data. Tests have been done by adopting forward, backward and central difference methods to determine the velocity gradient. No significant change (<5%) in gradients was observed and the backward difference method applied was defined as follows:

$$\left.\frac{\partial \overline{U}}{\partial y}\right|_{y=y_p} = \frac{\overline{U}|_{y=y_p} - \overline{U}|_{y=y_{p-1}}}{y_p - y_{p-1}} \quad (11)$$

where $\overline{U}|_{y=y_p}$ denotes the mean velocity at the point $y = y_p$.

3.4 Eddy viscosity

The eddy viscosity for combined wave-current flows was calculated as for a unidirectional turbulent current flow using definitions such as found in Pope (2000). The original definition of the eddy viscosity for a unidirectional turbulent current is given as follows, implying that eddy viscosity should have six components aligned with Reynolds stresses:

$$-\rho\overline{u_i' u_j'} = 2\mu_t\langle S_{ij}\rangle - \frac{2}{3}\rho k\delta_{ij} \quad (12a)$$

where $\langle S_{ij} \rangle$ is the rate-of-strain tensor defined as $\langle S_{ij} \rangle = \frac{1}{2}\left(\frac{\partial \langle u_i \rangle}{\partial x_j} + \frac{\partial \langle u_j \rangle}{\partial x_i}\right)$, μ_t is the turbulent dynamic viscosity which is related to eddy viscosity ε_t by the density of water, k is the turbulence kinetic energy (TKE) given by $k = \frac{1}{2}\left[(u')^2 + (v')^2 + (w')^2\right]$, and δ_{ij} is the Kronecker delta defined as $\delta_{ij} = \begin{cases} 0, & if\ i \neq j \\ 1, & if\ i = j \end{cases}$, with the suffixes i and j taking the value of 1, 2 or 3.

In the present study, only the eddy viscosity of most relevance to vertical diffusion was investigated. A 2D PIV system was adopted to obtain the velocity components in the streamwise and vertical directions. Thus, $\delta_{12} = 0$ and the original definition reduces to:

$$-\rho\overline{u'v'} = \mu_t \frac{\partial \bar{U}}{\partial y} \quad \text{..... (12b)}$$

where μ_t is the turbulent dynamic viscosity which is related to eddy viscosity ε_t by the density of water ρ.

The kinematic eddy viscosity ε_t can then be calculated as follows, based on Reynolds shear stress and mean velocity gradient obtained from the discrete experimental data：

$$\varepsilon_t|_{y=y_p} = \frac{\overline{\tau_{Rey}}|_{y=y_p}}{\rho * \frac{\partial \bar{U}}{\partial y}\Big|_{y=y_p}} \quad \text{.....(13)}$$

4. Experimental results

4.1 Semi-empirical formula of eddy viscosity distributions

PIV data collected from the wave-current flume and the low-turbulence flume are described below, showing profiles of mean velocity and Reynolds shear stress. These were used to calculate a semi-empirical formula for eddy viscosity.

4.1.1 Mean velocity profiles and mean velocity gradient

Figure 6 illustrates the vertical variation of mean velocity for all conditions tested in the wave-current flume. The choice of upper and lower limits for the logarithmic-profile region has a significant effect when selecting the best-fit line. Here, two main criteria were applied: i) to adopt the range that gives the best logarithmic-fitting quality as judged by the coefficient of determination R^2; ii) to set the upper boundary at the point where the mean velocity starts to deviate from the logarithmic profile. The criterion was set that if the discrepancy between the measurements and the logarithmic curve is more than 0.3%, then it was considered that the mean velocity was no longer logarithmic. Results for the unidirectional current indicate that a

logarithmic region exists in the bottom 30% of the boundary layer, giving an upper limit in accordance with that reported by Pope (2000). The Von Kármán constant was obtained from the logarithmic law of the wall, $\overline{U} = \frac{u_*}{\kappa} \ln\left(\frac{y}{y_0}\right)$. Here, u_* represents the shear velocity determined from bed shear stress measurements (u_{*c} and u_{*wc} represent the shear velocity for current-alone test and combined wave-current tests respectively), and y_0 is the apparent roughness, defined as the distance from the bed where the idealised logarithmic velocity profile becomes zero. In the next section, it is shown that $u_{*c} = 0.0078\ (\mathrm{m/s})$. Given this value, the Von Kármán constant κ=0.3. Many studies have been carried out to investigate the value of κ, although the canonical theory suggests the value of 0.4. The smooth pipe flow experiments of Nikuradse (1932) quote a range of κ from 0.32 to 0.43, over a variety of Reynolds numbers. Generally, the results presented above demonstrate that the turbulent current in the wave-current flume possesses the properties of a classical zero-pressure-gradient turbulent boundary layer and that the number of independent samples is adequate to produce statistically reliable results.

Applying the same approach to the unidirectional turbulent current condition in the low-turbulence flume, the value of the Von Kármán constant κ = 0.37. This is closer to the widely accepted value of 0.4. Aspect ratios, defined as the ratio of channel width to flow depth, are known to determine secondary flow responses and result in different values of κ. Given that the channel width of the low-turbulence flume was 0.49m and the water depth was 0.16m, the aspect ratio of the low-turbulence flume tests is 3. Therefore, secondary flows are weaker.

When waves are superimposed on the current, the most striking feature is that mean velocities are increased near the bed and decreased in the upper flow, as observed from earlier studies on wave-current interaction. The existence of logarithmic mean velocity profiles in combined wave-current flows is observed (shown by the blue lines in figure 6) in line with previous experiments reported for wave-current interaction (e.g., Trowbridge and Agrawal, 1995; Yuan and Madsen, 2015).

The mean velocity gradient is a key parameter in calculating experimental values for the eddy viscosity. Figure 7 shows the variations of mean velocity gradient versus the height above the bed in the wave-current flume, calculated using Equation (11). A consistent and substantial decrease in $d\overline{U}/dy$ caused by the waves is found in the outer flow region, while in the vicinity of the bed, $d\overline{U}/dy$ increases. The wave-induced reduction in the mean velocity gradient in the upper part is also observed in the low-turbulence flume and is in agreement with previous studies (e.g., Kemp and Simons, 1982; Klopman, 1994).

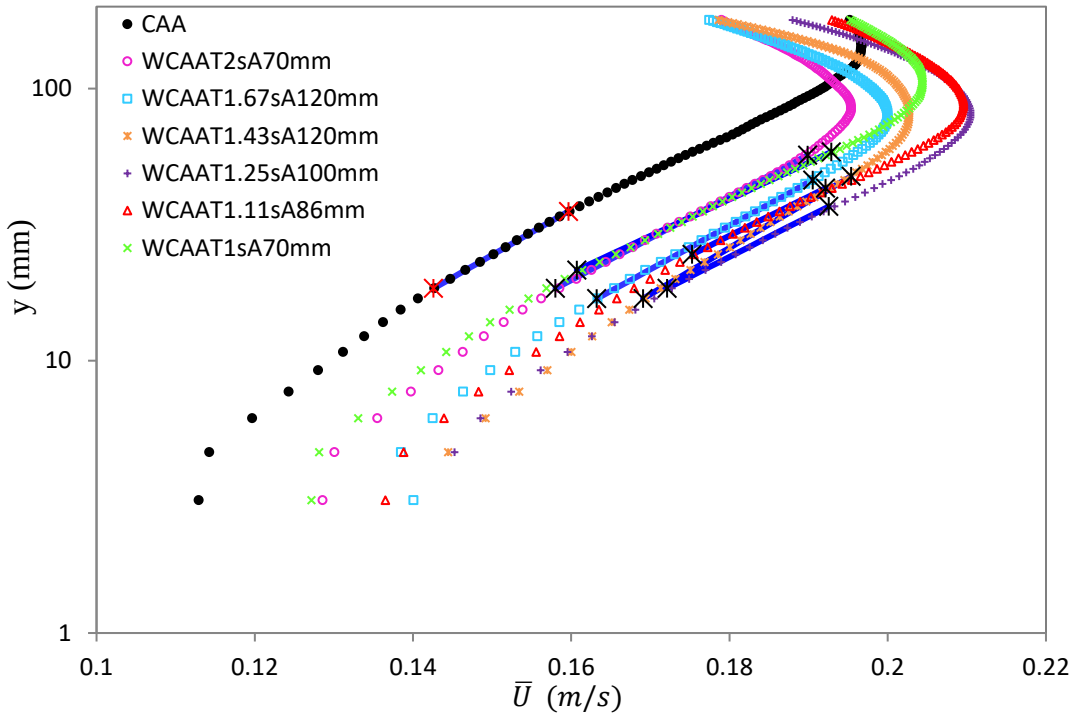

412
413 Figure 6. Mean velocity profiles of all test conditions in wave-current flume,
414 water depth $h = 0.4m$, flow rate of 0.178 (m/s), semi-logarithmic scale: 'CAA' for the
415 current-alone test; others for the combined wave-current tests.

416

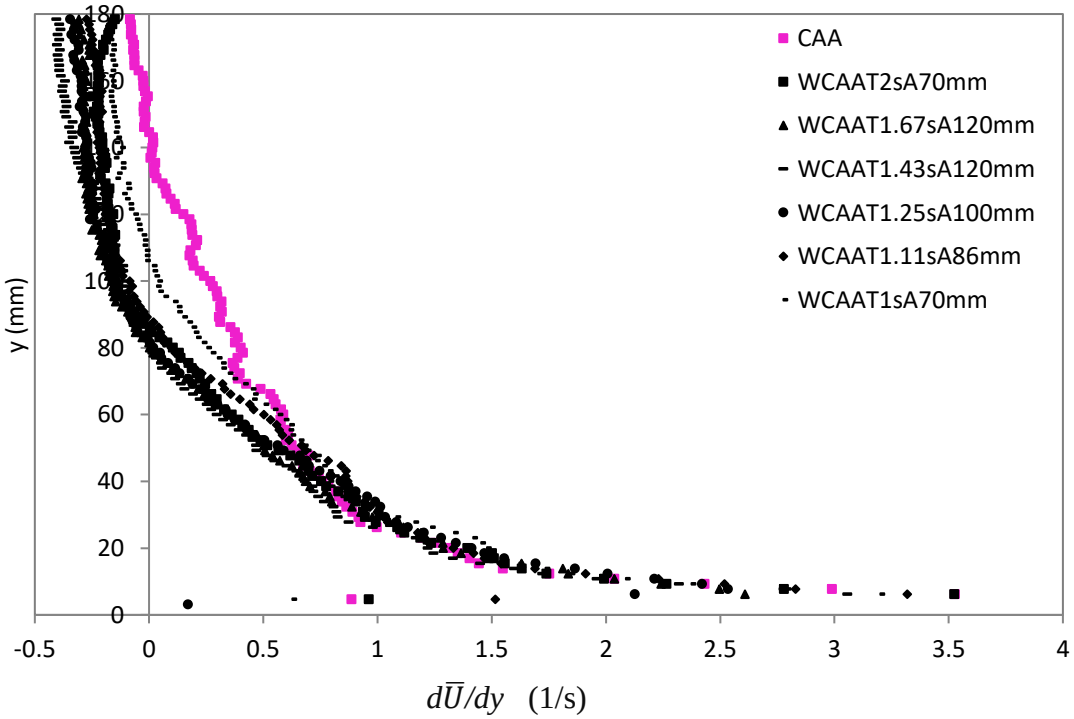

417
418 Figure 7. Vertical distribution of mean velocity gradient, all test conditions in the wave-
419 current flume, water depth $h = 0.4m$, flow rate of 0.178 (m/s).

420

4.1.2 Reynolds shear stress

An example of the bed shear stress and characteristic boundary layer length scale determination is given in Figure 8. Classical theory of turbulent boundary layers (Pope, 2000) indicates a linear distribution of Reynolds shear stress above the bottom viscous sublayer, based on the balance of forces. This is represented as $\tau(y) = \tau_{bc}(1 - y/\delta_c)$ and $\tau(y) = \tau_{bwc}(1 - y/\delta_{wc})$, where y represents the height above the smooth bed, τ_{bc} and τ_{bwc} are the bed shear stresses for the current-alone tests and for the combined wave-current tests respectively, δ_c and δ_{wc} are the characteristic boundary layer length scales for the current-alone tests and for the combined wave-current tests respectively. Applying the best-fit curve-fitting principle and using the aforementioned definitions, the characteristic boundary layer length scale is obtained as the height above the bed where Reynolds shear stress tends to zero. As can be seen, the linear fit is valid from around y=10mm. This is in agreement with classical theories of turbulent boundary layers. In the overlap region ($y^+ = \frac{y \cdot u_*}{\nu} > 50$ and $y/\delta_c < 0.1$), viscous and turbulent stresses are both important. The shear velocities for all tests are then calculated using the definition $u_{*c} = \sqrt{\frac{\tau_{bc}}{\rho}}$ and $u_{*wc} = \sqrt{\frac{\tau_{bwc}}{\rho}}$. Values of bed shear stress and characteristic boundary layer length scale are tabulated in Table 4 for those in the wave-current flume.

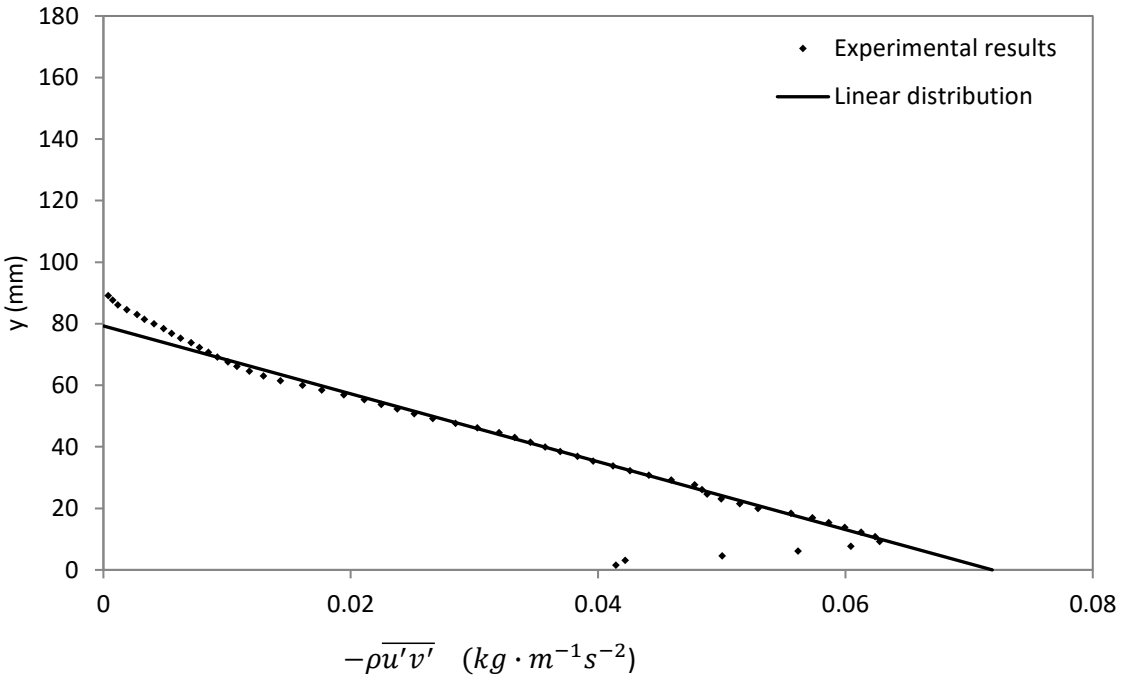

Figure 8. Vertical distribution of Reynolds shear stress and bed shear stress determination for the combined flow: *T*=1.11s, *A*=86mm, $h = 0.4m$, flow rate of 0.178 (m/s).

Table 4. Bed shear stress, shear velocities, and characteristic boundary layer length scale: turbulent currents with and without waves superimposed, water depth of 400mm, wave-current flume.

Test Condition	Bed shear stress τ_b $(kg \cdot m^{-1} \cdot s^{-2})$	Shear velocity $u_{*c}(\mathrm{m/s})$ and $u_{*\mathrm{wc}}(\mathrm{m/s})$	Characteristic boundary layer length scale $\delta_c(mm)$ and δ_{wc} (mm)
CAA	0.061	0.0078	143
WCAAT2sA70mm	0.063	0.0079	79
WCAAT1.67sA120mm	0.060	0.0078	75
WCAAT1.43sA120mm	0.063	0.0080	72
WCAAT1.25sA100mm	0.072	0.0085	69
WCAAT1.11sA86mm	0.072	0.0085	79
WCAAT1sA70mm	0.067	0.0082	102

4.1.3 Eddy viscosity

By analogy with the eddy viscosity concept in a unidirectional turbulent current, shear velocity can be used as the characteristic scaling parameter for non-dimensionalisation in wave-current flows. Physically, shear velocity is related to the orbital velocity of the vortices that create the turbulent mixing, exchange of particles and the momentum transfer across the boundary layer. It should be noted that the length scale for non-dimensionalisation adopted here is slightly different from previous studies of eddy viscosity. For a unidirectional turbulent current flow, Nezu and Rodi (1986) and Teles et al. (2013) used the water depth h as the scaling parameter. Previous models of wave-current interaction (Grant and Madsen, 1979; Christoffersen and Jonsson, 1985; You et al., 1991; Yuan and Madsen, 2015) also adopted the water depth as the scaling parameter for eddy viscosity, mainly because they assume a fully developed boundary layer with a high Reynolds number. However, in the present studies, a relatively low Reynolds number is involved, the flow is not always fully developed, and the addition of waves reduces the boundary layer thickness further. Therefore, the characteristic boundary layer length scale (δ_c and δ_{wc}) is more appropriate. This is demonstrated in Figure 9 and will be further discussed later.

The adoption of the velocity and length scales for the non-dimensionalisation of eddy viscosity as described above is consistent with classical turbulent boundary layer theory. Assuming that the velocity profile obeys the logarithmic law of the wall and that the Reynolds shear stress has a linear distribution, the kinematic eddy viscosity can be represented as $\varepsilon_t = \kappa \cdot u_* \cdot y \cdot (1 - y/\delta)$. Note that u_* is the shear velocity (u_{*c} for the current-only test and u_{*wc} for the combined wave-current condition), and δ represents the characteristic boundary layer length scale (δ_c for

the current-alone test and δ_{wc} for the combined wave-current condition). Thus, the non-dimensionalised eddy viscosity is found to be:

$$\varepsilon_t^+ = \frac{\varepsilon_t}{u_* \cdot \delta} = \kappa \cdot \frac{y}{\delta} \cdot \left(1 - \frac{y}{\delta}\right) \quad \text{.....(14)}$$

In the vicinity of the bed where the constant stress assumption is appropriate, the eddy viscosity should tend to a constant value (kinematic viscosity). However, in the fully turbulent regions of the boundary layer, the last term in Equation (14) is left out and the non-dimensional eddy viscosity is simplified as (Nielsen, 1992):

$$\varepsilon_t^+ = \kappa \cdot \frac{y}{\delta} \quad \text{.....(15)}$$

In this paper these two equations will be referred to as the analytical approach. The applicability of the equations is examined below.

The analytical approach agrees well with experimental results from the low-turbulence flume tests (Figure 9(a)); a linear distribution in the near-bed region and a parabolic one in the upper part of the water column with the transition point at $\frac{y}{\delta} = 0.1$. The value of the Von Kármán constant was determined from mean velocity profiles and Reynolds shear stress distributions. Reynolds shear stress estimation is presented in section 4.1.2. As can be seen from figure 9(b), results of eddy viscosities when non-dimensionalised using the water depth show considerable scatter and no clear linear and parabolic distributions. Figures 9(a) and 9(b) confirm that the characteristic boundary layer length scale is more appropriate than the water depth as the length parameter for non-dimensionalisation in the present study.

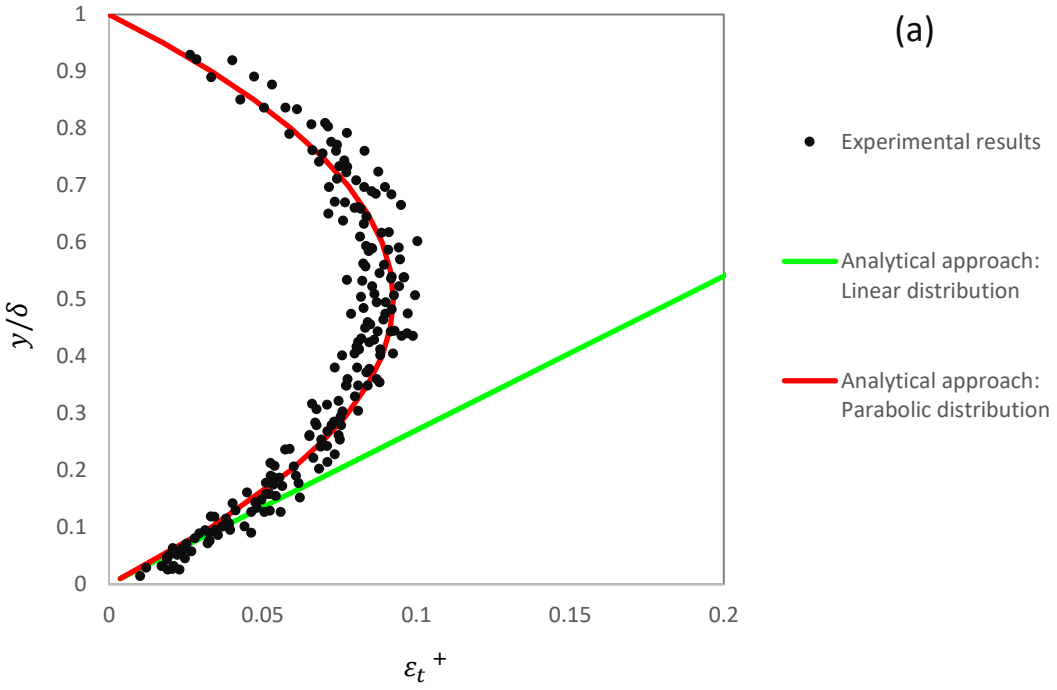

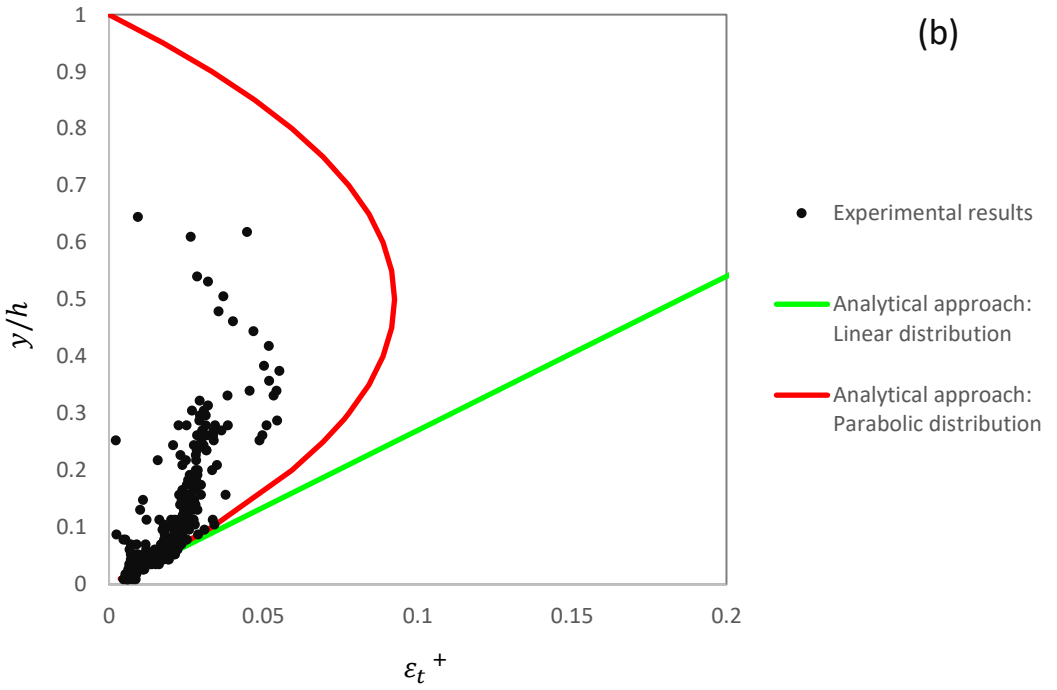

Figure 9. Distributions of non-dimensional eddy viscosity, tests conducted in the low-turbulence flume: (a) non-dimensionalised using the characteristic boundary layer length scales; (b) non-dimensionalised using the water depth.

However, the analytical approach does not always provide good agreement with experimental results from the wave-current flume tests. The experimental distribution of non-dimensional eddy viscosity appears to follow one of two types dependent on the relative strength of waves and currents, using the parameter adopted by Soulsby et al. (1993): type I (current-

dominated: $0.5 < \frac{\tau_c}{\tau_c + \tau_w} < 1$); and type II (wave-dominated: $0 < \frac{\tau_c}{\tau_c + \tau_w} \leq 0.5$) (Figure 10). The classification method was found to be in agreement with the previous study of Soulsby et al. (1993). In type I case conditions, the analytical approach provides a satisfactory agreement (Figure 10(a)): a linear distribution in the near-bed region and a parabolic one in the upper part, although there is some discrepancy. This may be caused by the fact that the boundary layer is still developing and from weak effects of the waves on the mean velocity gradient. The case for the current-alone condition lies in the first type. This is expected because unidirectional turbulent current can be considered as a limiting case. In type II case conditions, the analytical approach breaks down for $\frac{y}{\delta} \geq 0.4$ (Figure 10(b)). A linear distribution is observed in the experimental data in this region, represented as $\varepsilon_t^+ = a \cdot \left(\frac{y}{\delta}\right) + b$. To avoid a discontinuity at $\frac{y}{\delta} = 0.4$, the fitted curve is forced through the fixed point where $\frac{y}{\delta} = 0.4$ and $\varepsilon_t{}^+ = 0.24\kappa$, based on Equation (14). At the upper edge of the boundary layer, the non-dimensional eddy viscosity $\varepsilon_t{}^+$ is observed to have a value of 0.03 rather than the value of zero given by the analytical approach (plotted using the red line). Therefore, the coefficients a and b can be expressed as functions of the Von Kármán constant: $a = 0.05 - 0.4\kappa$; $b = 0.4\kappa - 0.02$.

Based on the findings above, the newly developed semi-empirical formula for non-dimensional eddy viscosity is represented as follows:

i). Type I (current-dominated)

$$\varepsilon_t{}^+ = \begin{cases} \kappa \cdot (\frac{y}{\delta}) & \frac{11.6\nu}{u_*} < \frac{y}{\delta} \leq 0.1 \\ \kappa \cdot \frac{y}{\delta} \cdot (1 - \frac{y}{\delta}) & 0.1 \leq \frac{y}{\delta} \leq 1 \end{cases} \quad \text{.....(16-a)}$$

ii). Type II (wave-dominated)

$$\varepsilon_t{}^+ = \begin{cases} \kappa \cdot \left(\frac{y}{\delta}\right) & \frac{11.6\nu}{u_*} < \frac{y}{\delta} \leq 0.1 \\ \kappa \cdot \frac{y}{\delta} \cdot \left(1 - \frac{y}{\delta}\right) & 0.1 \leq \frac{y}{\delta} \leq 0.4 \\ a \cdot (\frac{y}{\delta}) + b & 0.4 \leq \frac{y}{\delta} \leq 1 \end{cases} \quad \text{..... (16-b)}$$

where: $a = 0.05 - 0.4\kappa$; $b = 0.4\kappa - 0.02$.

The equations summarised above have implications for the structure of turbulence in wave-current interaction. When the waves superimposed are relatively small, their effect on the current is weak. The influence of the waves is apparent in the changes to shear velocities and boundary layer thickness, which are embedded in the non-dimensionalisation analysis of eddy viscosities. Therefore, non-dimensional eddy viscosity distributions have the same mathematical representation as those of unidirectional turbulent currents. However, under conditions with large waves, re-laminarisation can occur as explained in the investigation of

Lodahl et al. (1998). Turbulence in the outer region is significantly inhibited by the waves and the processes of turbulent mixing are inhibited accordingly. This leads to a linear distribution of non-dimensional eddy viscosity.

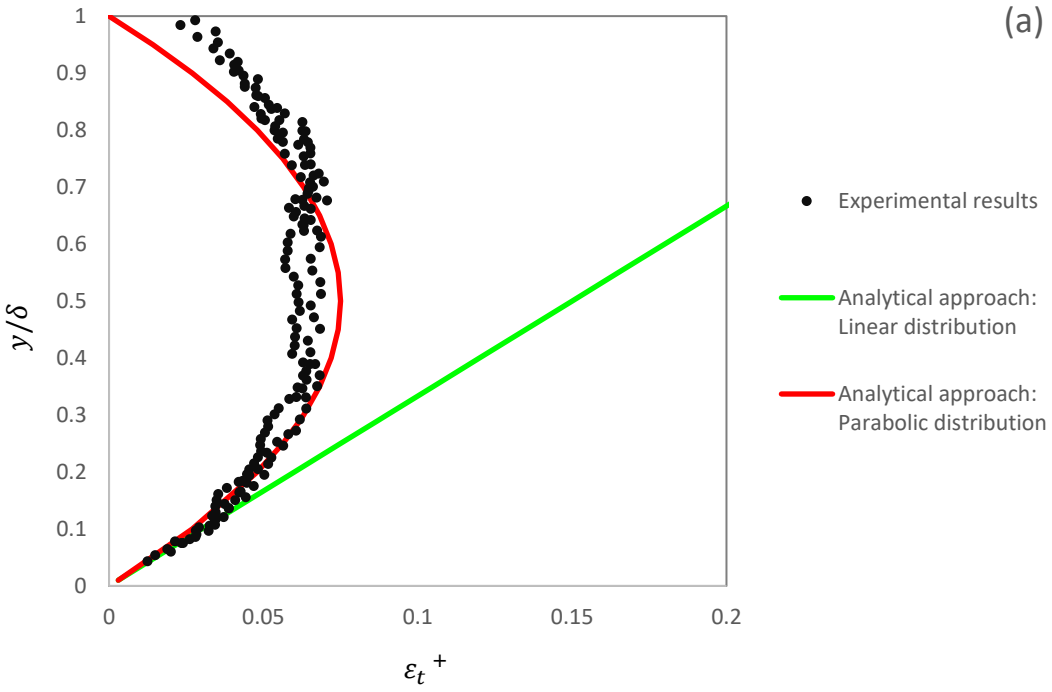

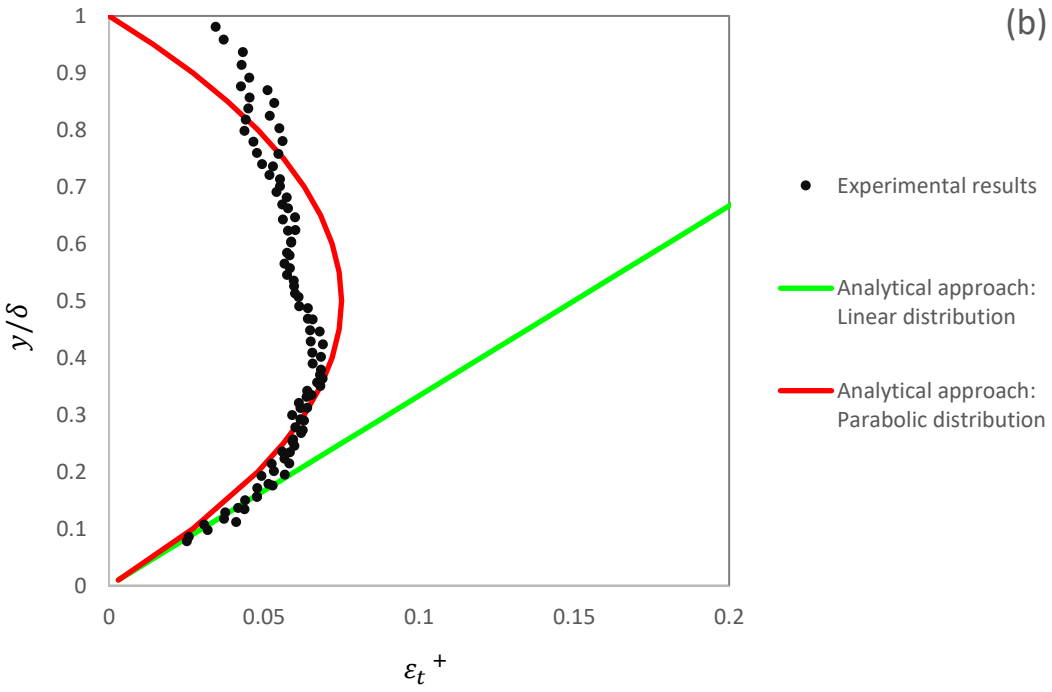

Figure 10. Distributions of non-dimensional eddy viscosity, tests conducted in the wave-current flume: (a) type I; (b) type II.

A comparison with other eddy viscosity distributions is presented in Figure 11. Note that the Grant and Madsen (1979) model uses the formula: $\varepsilon_t = \begin{cases} \kappa \cdot u_{*_{wc}} \cdot y & , \ y > \delta_w \\ \kappa \cdot u_{*_{wcm}} \cdot y & , \ y < \delta_w \end{cases}$ where δ_w represents the wave boundary layer thickness and $u_{*_{wcm}} = \sqrt{\tau_{bmax}/\rho}$ with τ_{bmax} for the maximum value of bed shear stress within one wave cycle. Results show that the model of Grant and Madsen (1979) overestimates the eddy viscosity in the outer flow. The model of Yuan and Madsen (2015) was a modification of Grant and Madsen (1979) avoiding the discontinuity of eddy viscosity between the inner and outer layers. Hence, the general shape is the same as for Grant and Madsen (1979) and therefore is not included here. The model given by Christoffersen and Jonsson (1985), for a relatively small roughness (named as 'Model II' in their original paper), is presented as the 'Christoffersen and Jonsson (1985) – original' in the figure. The values predicted using their model were calculated by the formula: $\varepsilon_t = \begin{cases} \kappa \cdot y \cdot u_{*_{wc}} \cdot (1 - y/h) & , \ \delta_w < y < h \\ \kappa \cdot u_{*_{wcm}} \cdot y & , \ y \leq \delta_w \end{cases}$. This model again overestimates the observed eddy viscosity distribution in the outer flow in the present data. This is because the Christoffersen and Jonsson (1985) model assumes eddy viscosity has a parabolic distribution throughout the water depth, while the present experimental data indicate that the length scale for the combined flow should be the thickness of the boundary layer. However, the Christoffersen and Jonsson (1985) model is based on a fully developed boundary layer assumption, which is not the case in the present study. The 'Christoffersen and Jonsson (1985) – Adapted' plot in Figure 11 re-scales their original model using the observed characteristic boundary layer length scale. This shows their model to work well near the bed, but to differ slightly from the present formula in the upper region. It should be noted that the Grant and Madsen (1979) model does not contain the water depth in their formula, hence their model cannot be re-scaled in the same way as the adapted version of Christoffersen and Jonsson (1985).

Although there has been debate as to whether turbulent eddy viscosity in an oscillatory flow should be time-invariant or time-dependent, the experimental data presented here suggest that a time-invariant eddy viscosity model can describe mean flow kinematics in most cases in a combined wave-current flow. However, it should be noted that if a prediction of second order drift quantities such as streaming is required, a time-dependent turbulent boundary layer needs to be modelled and then averaged. In that case, a time-dependent eddy viscosity is necessary. A time-independent eddy viscosity best reflects the turbulent coherent structures and vortices that persist within the boundary layer. Turbulent loops under the effects of wave motions

convect with the mean flow, and may also undergo deformations during deceleration and acceleration phases. Although these turbulent vortices may vary in scale within one wave cycle, the shape of the turbulent boundary layer is retained. Previous research (e.g., Grant and Madsen, 1979; You et al., 1991; Yuan and Madsen, 2015) has pointed out that a time-varying eddy viscosity would call for numerical approaches rather than analytical methods, in order to solve the governing equations. Therefore, in a practical sense, the adoption of a time-varying eddy viscosity for two-dimensional and three-dimensional simulations would be demanding on computational resources.

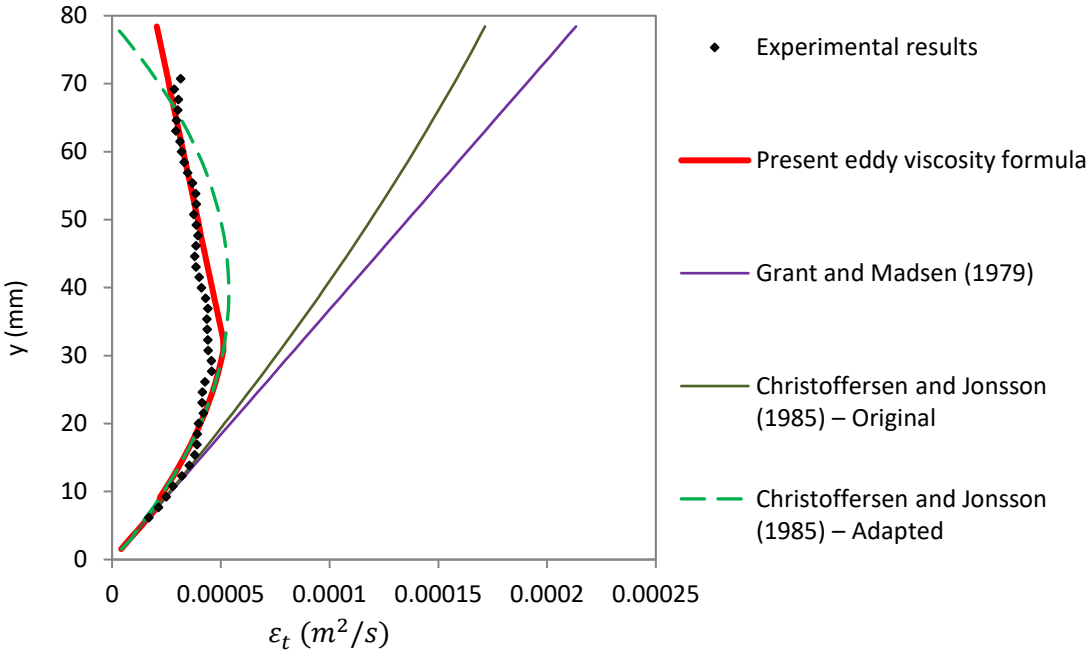

Figure 11. Eddy viscosity distribution of combined wave-current flow: *T=1.11s*, *A=86mm*, *h= 0.4m*, flow rate of 0.178 (m/s), wave-current flume.

4.2 Validation of the semi-empirical formula

In order to investigate the wider validity of the present semi-empirical formula (Equations 16-a and 16-b), a comparison has been made with the experimental results from the large oscillating water tunnel tests. These tests considered combined wave-current flows with high wave-Reynolds number over a wide range of oscillatory periods (2.75s to 9.5s) and amplitudes (0.24m to 0.62m) (Table 3). Note that all conditions lie within the type II eddy viscosity distribution. The present semi-empirical formula for eddy viscosity was proposed for combined flows over a smooth bed. However, the comparison shown in Figure 12 demonstrates that it is also valid for flows over rough boundaries. This is consistent with work by Grass (1971) which showed

588 that the turbulent boundary layer above the near-bed layer is the same over smooth and rough
589 beds.
590 It should be noted that: the eddy viscosity was normalised by the product of the characteristic
591 length scale δ_{wc} and the shear velocity u_{*wc} of the combined wave-current flow obtained
592 directly from the shear plate; the height above the roughness element crest was normalised by
593 the characteristic length scale to show the relative vertical position within the boundary layer;
594 and, the Von Kármán constant was found to be 0.3 by applying the logarithmic law.
595 The combined flows in an oscillating water tunnel simulate many aspects of wave-current flow
596 in the lower part of the boundary layer at near full-scale ocean conditions. Oscillating water
597 tunnels can generate large orbital amplitudes and oscillation periods, with great control,
598 producing high wave-Reynolds number flows similar to ocean conditions, thereby overcoming
599 several physical limitations inherent in laboratory-scale wave flumes. This feature makes it
600 reasonable to generalise the present findings and consider the proposed semi-empirical formula
601 is applicable to real ocean sites.

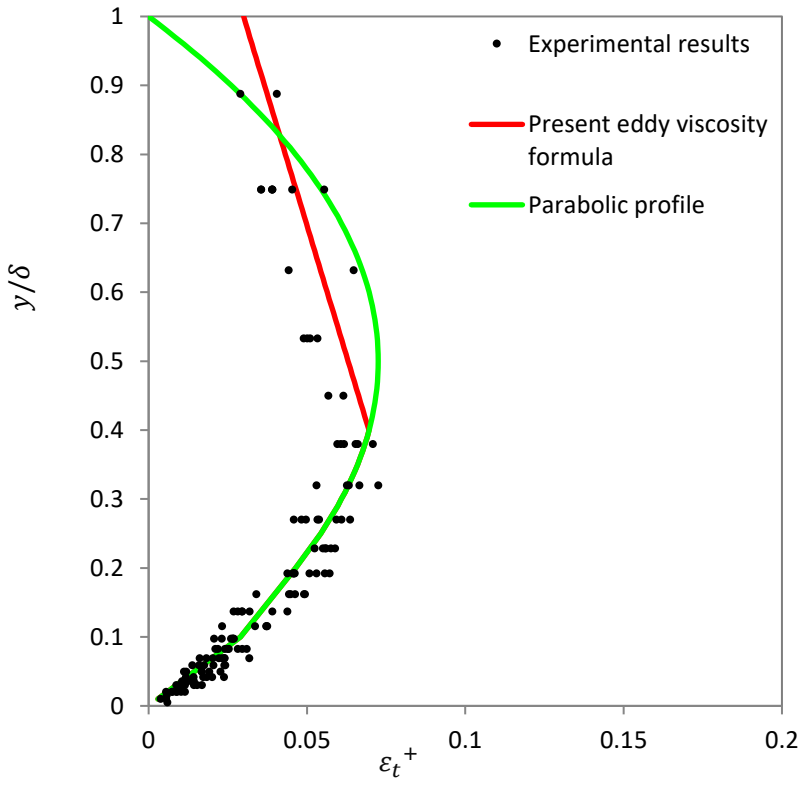

602
603 Figure 12. Vertical profiles of non-dimensional mean eddy viscosity for all tests conducted in
604 the Large Oscillating Water Tunnel.
605

5. Discussions

The consequence for the mean velocity profile of the different eddy viscosity distributions plotted in Figure 11 is shown in Figure 13, based on the governing equation $\frac{\partial \bar{U}}{\partial y} = \frac{(u_{*wc})^2\,(1-y/h)}{\varepsilon_t}$ or $\frac{\partial \bar{U}}{\partial y} = \frac{(u_{*wc})^2\,(1-y/\delta_{wc})}{\varepsilon_t}$. It should be pointed out here that the first equation is in the same form as given by You (1994), while the second one is found by substituting the typical length scale δ_{wc} for water depth h. The first equation was derived by combining the two basic equations:

$$\tau(y) = \rho(u_{*wc})^2\left(1-\frac{y}{h}\right) \quad \ldots\ldots (17)$$

$$\frac{\tau(y)}{\rho} = \varepsilon_t \cdot \frac{\partial \bar{U}}{\partial y} \quad \ldots\ldots (18)$$

For those models where a fully developed turbulent boundary layer is assumed, the first equation is adopted. For the other models, the change is made because Reynolds shear stress reaches zero at the edge of the boundary layer rather than at the free surface.

The figure demonstrates that, in the lower water column, the mean velocities predicted using the eddy viscosity distributions of Grant and Madsen (1979), Christoffersen and Jonsson (1985) and the distribution proposed here are all in good agreement with the experimental data obtained from the wave-current flume.

However, above $y^+ = 300$, the velocity profiles predicted using the eddy viscosity distributions from Grant and Madsen (1979) and Christoffersen and Jonsson (1985) both underestimate the observed mean velocity. This is explained by the divergence of values for ε_t in the upper water column, as shown in Figure 11.

Mean velocities predicted using the adapted version of Christoffersen and Jonsson (1985) are also observed to underestimate the experimental results. This is not surprising since although the adapted version of their model is based on the characteristic length scale of the boundary layer, the parabolic distribution of eddy viscosity mathematically leads to a logarithmic velocity profile. Therefore, this distribution cannot accurately describe the mean velocity profile for those regions where logarithmic laws are not obeyed.

It should be pointed out here that although the discrepancy between the mean velocity profiles determined from different eddy viscosity distributions is not large, the eddy viscosity distribution proposed in this paper is more accurate for describing the flow kinematics in the upper flow region.

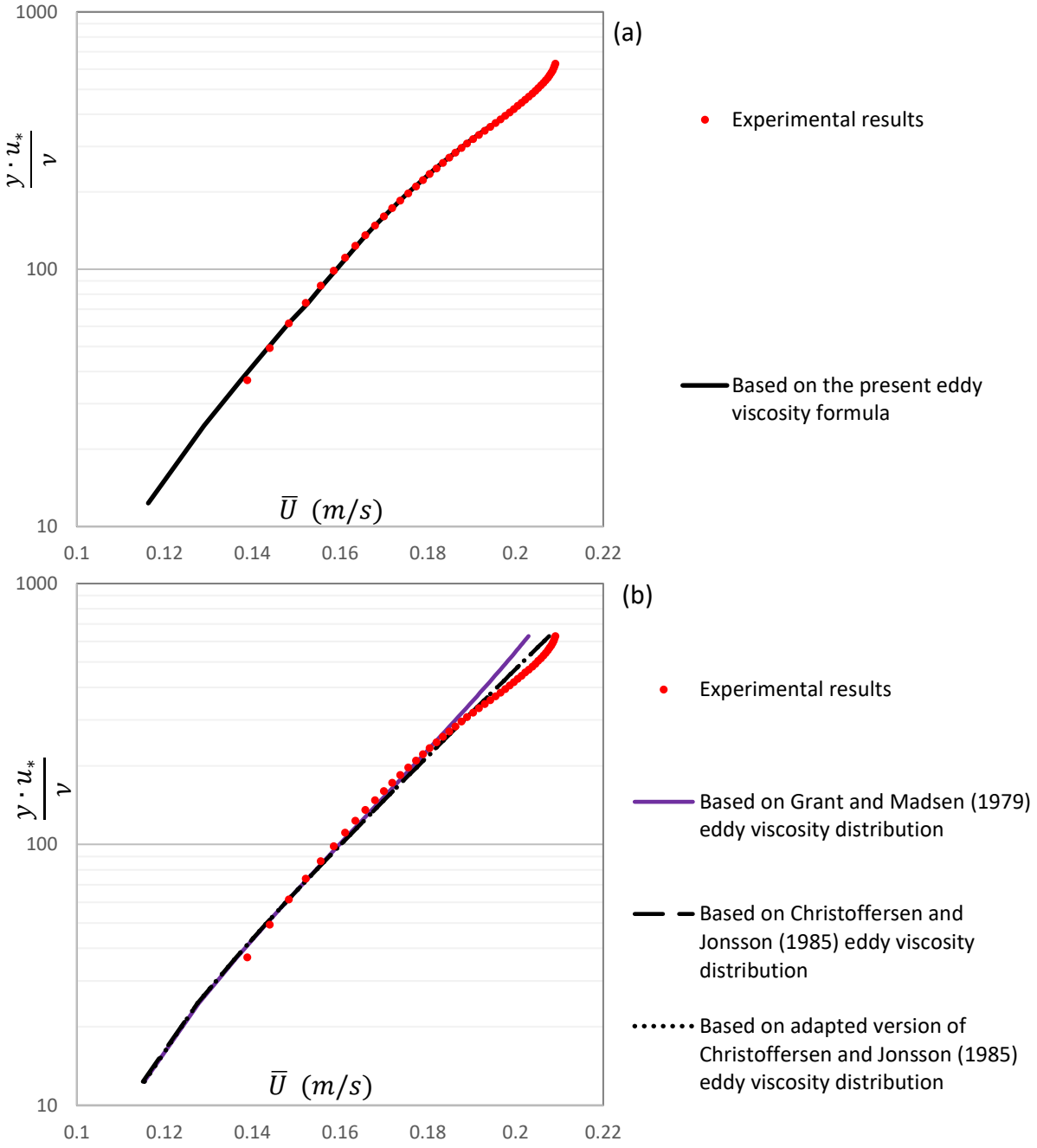

Figure 13. Intercomparison of the mean velocity profiles, based on various eddy viscosity assumptions. Combined flow over a smooth bed, T=1.11s, A=86mm, $h = 0.4$m, flow rate of 0.178 (m/s), wave-current flume: (a) based on the present eddy viscosity formula; (b) based on previous eddy viscosity assumptions.

6. Concluding remarks

Results from experiments in three different facilities, a large oscillating water tunnel and two wave-current flumes, have been analysed. A new semi-empirical formula has been put forward for the eddy viscosity distribution in a combined wave-current flow. Experimental results from the oscillating water tunnel have been used to validate the formula and suggest robust

performance. This new eddy viscosity distribution has been shown to represent real conditions better than previous eddy viscosity assumptions. Its range of validity includes both small-scale, low Reynolds number, and large-scale, high Reynolds number conditions and is applicable over smooth and rough boundaries.

An important application of the proposed eddy viscosity distribution is giving guidance to numerical modellers. The proposed eddy viscosity distribution is valuable for large-scale simulations of coastal flow, including sediment transport, where solving the detailed seabed boundary layer using two-equation models (e.g. $k-\varepsilon$ and $k-\omega$ models) is not practical due to the large computational effort that would be required in three-dimensional simulations. Here we should emphasize that the eddy viscosity model proposed in this paper is for the mean flow. It does not give an instantaneous eddy viscosity related to the wave phase (e.g., during the passage of a wave crest), which would vary with time.

Another important application of eddy viscosity is in sediment transport. The sediment diffusion coefficient is related to the eddy viscosity profile, and therefore a more accurate mathematical representation is significant in calculating the vertical diffusion coefficient of any suspended sediment.

List of Symbols

Symbol	Description
U_w	Amplitude of streamwise velocity just outside the bottom oscillatory boundary layer
a_w	Orbital amplitude of fluid just outside the bottom oscillatory boundary layer
Re_w	Amplitude Reynolds number
U_c	Depth-averaged mean velocity
$U_{\infty c}$	Current free-stream velocity
Re_c	Current Reynolds number
T	Wave period
H	Wave height
L	Wave length
A	Wave amplitude
a	Coefficient, represented as a function of the Von Kármán constant
b	Coefficient, represented as a function of the Von Kármán constant
κ	Von Kármán constant
k_s	Nikuradse roughness parameter

Symbol	Description
ε_t	Eddy viscosity
h	Water depth
i	Index number of positions in the x direction
M	Instantaneous velocity component (representing u, v, or w)
u	Instantaneous streamwise velocity
v	Instantaneous vertical velocity
w	Instantaneous spanwise velocity
N_1	Number of measurements for time-averaging
N_2	Number of periods for ensemble-averaging
dt	Time between two consecutive measurements
t	Time sequence
f	Sampling frequency
x	Horizontal displacement
	Vertical displacement above the bed
z	Transverse displacement
M_{new}	Spatially averaged velocities within three adjacent points in the x direction
ρ	Density of water
ν	Kinematic viscosity of water
$\overline{U}$	Mean velocity
$\langle S_{ij} \rangle$	Rate-of-strain tensor
μ_t	Turbulent dynamic viscosity
δ_{ij}	Kronecker delta
k	Turbulence kinetic energy (TKE)
u_*	Shear velocity, either in a current-alone condition (u_{*c}) or a combined wave-current flow (u_{*wc}).
u_{*wcm}	Maximum value of shear velocity within one wave cycle
R^2	Coefficient of determination
$\overline{\tau_{Rey}}$	Reynolds shear stress
τ_b	Bed shear stress, either in a current-alone condition (τ_{bc}) or a combined wave-current flow (τ_{bwc}).
τ_{bmax}	Maximum value of bed shear stress within one wave cycle
δ_w	Wave boundary layer thickness
δ_c	Characteristic boundary layer length scale of the unidirectional current

Symbol	Description
δ_{wc}	Characteristic boundary layer length scale of the combined wave-current flows
ε_t^+	Non-dimensional eddy viscosity

Operators	Description
$\bar{M}$	Time-average of M over the whole sampling period
M'	Turbulence fluctuations component of M
$\widetilde{M}$	Periodic component of M with $\bar{M}$ subtracted
$\langle M \rangle$	Ensemble-average of M

Acknowledgments

The authors gratefully appreciate for the financial support from the UCL Dean's Prize and the China Scholarship Council (CSC). This work was supported by the National Natural Science Foundation of China (Grant No. 51909074) and China Postdoctoral Science Foundation (Grant No. 2019M661713), the Fundamental Research Funds for the Central Universities (B210202024), and Key Laboratory of Coastal Disaster and Defence of Ministry of Education, Hohai University (Grant No. 201912). We are grateful to Dr. Jan Ribberink for providing the valuable experimental data from the De Voorst Laboratory of Delft Hydraulics.

References

1. Bakker, W., and van Doorn, T., 1978. Near-bottom velocities in waves with a current. Proc. 16th Coastal Engng. Conf., Hamburg, ASCE, 82, 1394-1413.
2. Boussinesq, J., 1877. "Essai sur la théorie des eaux courantes", Mémoires présentés par divers savants à l'Académie des Sciences, 23, 1-680.
3. Christoffersen, J.B. and Jonsson, I.G., 1985. Bed friction and dissipation in a combined current and wave motion. Ocean Engineering, 12, 387-423.
4. Clauser, F.H., 1956. The turbulent boundary layer. In Advances in applied mechanics, 4, 1-51. Elsevier.
5. Davies, A.G., Soulsby, R.L., and King, H.L., 1988. A numerical model of the combined wave and current bottom boundary layer. Journal of Geophysical Research, 93, 491-508.

6. Egan, G., Manning, A.J., Chang, G., Fringer, O. and Monismith, S., 2020. Sediment-induced stratification in an estuarine bottom boundary layer. Journal of Geophysical Research: Oceans, 125(8), p.e2019JC016022.
7. Fernando, P.C., Guo, J. and Lin, P., 2011. Wave–current interaction at an angle 1: experiment. Journal of Hydraulic Research, 49, 424-436.
8. Fredsøe, J., 1984. Turbulent boundary layer in wave-current motion. Journal of Hydraulic Engineering, 110, 1103-1120.
9. Fredsøe, J., Andersen, K.H., Sumer, B.M., 1999. Wave plus current over a ripple-covered bed. Coastal Engineering, 38, 177-221.
10. Grant, W.D. and Madsen, O.S. 1979. Combined Wave and Current Interaction with a Rough Bottom. Journal of Geophysical Research, 84, 1797-1808.
11. Grass, A.J., 1971. Structural features of turbulent flow over smooth and rough boundaries. Journal of Fluid Mechanics, 50, 233-255.
12. Holmedal, L.E., Myrhaug, D., Rue, H., 2000. Seabed shear stresses under irregular waves plus current from Monte Carlo simulations of parameterized models, Coastal Engineering, 39, 123-147.
13. Holmedal, L.E., Myrhaug, D., Rue, H., 2003. The sea bed boundary layer under random waves plus current. Continental Shelf Research, 23, 717–750.
14. Huntley, D.A. and Hazen, D.G., 1988. Seabed stresses in combined wave and steady flow conditions on the Nova Scotia continental shelf: Field measurements and predictions. Journal of Physical Oceanography, 18, 347-362.
15. Jepsen, R.A., Roberts, J.D., Kearney, S.P., Dimiduk, T.G., O'Hern, T.J. and Gailani, J.Z., 2011. Shear stress measurements and erosion implications for wave and combined wave-current generated flows. Journal of Waterway, Port, Coastal, and Ocean Engineering, 138, 323-329.
16. Kemp, P. H. and Simons, R. R. 1982. The interaction between waves and a turbulent current: waves propagating with the current. Journal of Fluid Mechanics, 116, 227-250.
17. Kemp, P. H. and Simons, R. R. 1983. The interaction of waves and a turbulent current: waves propagating against the current. Journal of Fluid Mechanics, 130, 73-89.
18. Klopman, G., 1994. Vertical structure of the flow due to waves and currents: laser-Doppler flow measurements for waves following or opposing a current. Tech. Rep. Delft Hydraulics H840.32.

19. Lambrakos, K.F., Myrhaug, D. and Siaattelid, O.H., 1988. Seabed current boundary layers in wave-plus-current flow conditions. Journal of Waterway, Port, Coastal, and Ocean Engineering, 114, 161-174.
20. Lodahl, C.R., Sumer, B.M. and Fredsøe, J., 1998. Turbulent combined oscillatory flow and current in a pipe. Journal of Fluid Mechanics, 373, 313-348.
21. Lundgren, H., 1972. Turbulent currents in the presence of waves. Proc. 13th Coastal Engng. Conf., Vancouver, ASCE, chapter 33, 623-634.
22. Malarkey, J., Davies, A.G., 1998. Modelling wave–current interactions in rough turbulent bottom boundary layers. Ocean Engineering, 25, 119–141.
23. Musumeci, R.E., Cavallaro, L., Foti, E., Scandura, P. and Blondeaux, P., 2006. Waves plus currents crossing at a right angle: Experimental investigation. Journal of Geophysical Research: Oceans, 111(C7).
24. Myrhaug, D., 1982. On a theoretical model of rough turbulent wave boundary layers. Ocean Engineering, 9(6), 547-565.
25. Myrhaug, D. and Slaattelid, O.H., 1989. Combined wave and current boundary layer model for fixed rough seabeds. Ocean engineering, 16(2), 119-142.
26. Myrhaug, D. and Slaattelid, O.H. 1990. A rational approach to wave-current friction coefficients for rough, smooth and transitional turbulent flow. Coastal Engineering, 14, 265-293.
27. Nezu, I and Rodi, W, 1986. Open-channel flow measurements with a laser Doppler anemometer. Journal of Hydraulic Engineering, 112(5):335-355.
28. Nielsen, P., 1992. Coastal bottom boundary layers and sediment transport.
29. Perry, A.E. and Joubert P.N., 1963. Rough-wall boundary layers in adverse pressure gradients. Journal of Fluid Mechanics, 17, 193-211.
30. Perry, A.E., Schofield, W.H., and Joubert P.N., 1969. Rough wall turbulent boundary layers. Journal of Fluid Mechanics, 37, 383-413.
31. Pope, S.B., 2000. Turbulent flows. Cambridge University Press, Cambridge, U.K.
32. Silva, M.C., Vitola, M.A., Esperança, P.T.T., Sphaier, S.H. and Levi, C.A., 2016. Numerical simulations of wave–current flow in an ocean basin. Applied Ocean Research, 61, pp.32-41.
33. Simons, R.R. and MacIver, R.D., 2001. Regular, bichromatic and random waves on co-linear currents. Coastal Dynamics' 01, 132-141.

751 34. Simons, R.R., Grass, T.J., Tehrani, M.M., 1992. Bottom shear stresses in the boundary
752 layers under waves and currents crossing at right angles. Coastal Engineering, 45, 604-
753 617.
754 35. Simons, R.R., Grass, T.J., Saleh, W.M., Tehrani, M.M., 1994. Bottom shear stresses
755 under random waves with a current superimposed. Coastal Engineering, 42, 565-578.
756 36. Simons, R.R., Myrhaug, D., Thais, L., Chapalain,G., Holmedal, L.E., and MacIver, R.,
757 2000. Bed friction in combined wave-current flows. Coastal Engineering, 216-226.
758 37. Sleath, J.F., 1984. Sea bed mechanics.
759 38. Son, H.T. and Andre, T.., 1991. A numerical model of the rough turbulent boundary
760 layer in combined wave and current interaction. In Coastal Engineering 1990, 853-866.
761 39. Soulsby, R.L., Hamm, L., Klopman, G., Myrhaug, D., Simons, R.R., and Thomas, G.P.
762 1993. Wave-current interaction within and outside the bottom boundary layer. Coastal
763 Engineering, 21, 41–69.
764 40. Soulsby, R. L. and Humphrey, J. D. (1990) Field observations of wave–current
765 interaction at the sea bed. In Proceedings of the NATO Advanced Research Workshop
766 on Water Wave Kinematics, ed. A. Tørum and O. T. Grudmestad, 413–428. Kluwer,
767 Dordrecht.
768 41. Stuart, R.J., 1984. Three-dimensional characteristics of coherent flow structures in a
769 turbulent boundary layer over a rough surface. Ph.D. Thesis, University of London.
770 42. Teles, M. J., Pires-Silva, A., and Benoit, M., 2012. The influence of the turbulence
771 closure model on wave-current interaction modelling at a local scale. Proceedings of
772 33rd Conference on Coastal Engineering, Santander, Spain, 1-12.
773 43. Teles, M.J., Pires-Silva, A.A., Benoit, M., 2013. Numerical modelling of wave current
774 interactions at a local scale. Ocean Modelling, 68, 72–87.
775 44. Trowbridge, J.H. and Agrawal, Y.C., 1995. Glimpses of a wave boundary layer. Journal
776 of Geophysical Research: Oceans, 100, 20729-20743.
777 45. Umeyama, M., 2005. Reynolds Stresses and Velocity Distributions in a Wave-Current
778 Coexisting Environment. Journal of Waterway, Port, Coastal, and Ocean engineering,
779 131, 203-212.
780 46. Umeyama, M., 2009. Changes in Turbulent Flow Structure under Combined Wave-
781 Current Motions. Journal of Waterway, Port, Coastal, and Ocean Engineering, 135,
782 213–227.

47. Umeyama, M., 2011. Coupled PIV and PTV Measurements of Particle Velocities and Trajectories for Surface Waves Following a Steady Current. Journal of Waterway, Port, Coastal, and Ocean Engineering, 137, 85–94.
48. Van Doorn, T., 1981. Experimental investigation of near-bottom velocities in water waves without and with a current. Delft Hydraulics Laboratory (No. M143). Report.
49. You, Z.J., Wilkinson, D.L. and Nielsen, P., 1991. Velocity distributions of waves and currents in the combined flow. Coastal Engineering, 15, 525-543.
50. You, Z.J., Wilkinson, D.L., and Nielsen, P., 1992. Velocity distribution in turbulent oscillatory boundary layer. Coastal engineering, 18, 21-38.
51. You, Z.J., 1994. A simple model for current velocity profiles in combined wave-current flows. Coastal Engineering, 23, 289-304.
52. Yuan, J. and Madsen, O.S., 2014. Experimental study of turbulent oscillatory boundary layers in an oscillating water tunnel. Coastal Engineering, 89, 63-84.
53. Yuan, J. and Madsen, O.S., 2015. Experimental and theoretical study of wave–current turbulent boundary layers. Journal of Fluid Mechanics, 765, 480-523.
54. Zhang, J.S., Zhang, Y., Jeng, D.S., Liu, P.L.F., Zhang, C. 2014. Numerical simulation of wave–current interaction using a RANS solver. Ocean Engineering, 75, 157-164.
55. Zhang, X., Simons, R., Buldakov, E., 2017. A numerical study of wave-current interaction in the bottom boundary layer. Proceedings of 35th Conference on Coastal Engineering, Antalya, Turkey, 2016.
56. Zhang, X. and Simons, R., 2019. Experimental investigation on the structure of turbulence in the bottom wave-current boundary layers. Coastal Engineering, 152, p.103511.
57. Zheng, J., Zhang, C., Wang, Y. and Demirbilek, Z., 2011. Improvement of bottom boundary layers modeling under interactions of wave and wave-induced current. Coastal Engineering Proceedings, 1, 46.
58. Zitman, T.J. and Schuttelaars, H.M., 2012. Importance of cross-channel bathymetry and eddy viscosity parameterisation in modelling estuarine flow. Ocean Dynamics, 62(4), pp.603-631.